



Article

A Multi-Level Robust Positioning Method for Three-Dimensional Ground Penetrating Radar (3D GPR) Road Underground Imaging in Dense Urban Areas

Ju Zhang ^{1,2}, Qingwu Hu ^{3,*}, Yemei Zhou ¹, Pengcheng Zhao ³ and Xuzhe Duan ³

¹ School of Engineering and Architecture, Wuhan City Polytechnic, Wuhan 430072, China; zhangju@whu.edu.cn (J.Z.); 02009001@whcp.edu.cn (Y.Z.)

² Key Laboratory of National Geographic Census and Monitoring, Ministry of Natural Resources, Wuhan 430072, China

³ School of Remote Sensing and Information Engineering, Wuhan University, Wuhan 430079, China; pengcheng.zhao@whu.edu.cn (P.Z.); duanxz@whu.edu.cn (X.D.)

* Correspondence: huqw@whu.edu.cn

Abstract: Three-Dimensional Ground Penetrating Radar (3D GPR) detects subsurface targets non-destructively, rapidly, and continuously. The complex environment around urban roads affects the positioning accuracy of 3D GPR. The positioning accuracy directly affects the data quality, as inaccurate positioning can lead to distortion and misalignment of 3D GPR data. This paper proposed a multi-level robust positioning method to improve the positioning accuracy of 3D GPR in dense urban areas in order to obtain more accurate underground data. In environments with good GNSS signals, fast and high-precision positioning can be achieved based on GNSS data using differential GNSS technology; in scenes with weak GNSS signals, high-precision positioning of subsurface data can be achieved by using GNSS and IMU as well as using GNSS/INS tightly coupled solution technology; in scenes with no GNSS signals, SLAM technology is used for positioning based on INS data and 3D point cloud data. In summary, this method ensures a positioning accuracy of 3D GPR better than 10 cm and high-quality 3D images of underground urban roads in any environment. This provides data support for urban road underground structure surveys and has broad application prospects in underground disease detection and prevention.

Keywords: multi-level robust positioning method; 3D ground penetrating radar; 3D mobile survey system; laser SLAM positioning



Citation: Zhang, J.; Hu, Q.; Zhou, Y.; Zhao, P.; Duan, X. A Multi-Level Robust Positioning Method for Three-Dimensional Ground Penetrating Radar (3D GPR) Road Underground Imaging in Dense Urban Areas. *Remote Sens.* **2024**, *16*, 1559. <https://doi.org/10.3390/rs16091559>

Academic Editor: David Gomez-Ortiz

Received: 28 February 2024

Revised: 18 April 2024

Accepted: 20 April 2024

Published: 27 April 2024



Copyright: © 2024 by the authors. Licensee MDPI, Basel, Switzerland. This article is an open access article distributed under the terms and conditions of the Creative Commons Attribution (CC BY) license (<https://creativecommons.org/licenses/by/4.0/>).

1. Introduction

Ground Penetrating Radar (GPR) is one of the non-destructive measurement techniques that uses electromagnetic waves to locate objects or interfaces buried within visually opaque material or underground. GPR transmits a regular sequence of low-power electromagnetic energy to the material or ground and receives and surveys weak reflected signals from buried objects. GPR uses electromagnetic waves to respond to changes in the electromagnetic properties of the shallow subsurface. The propagation velocity of electromagnetic waves is the main controlling factor in generating reflections; it is determined by the relative dielectric constant contrast between the background material and the object. The GPR method is a rapid, nondestructive, high-accuracy, continuous, and high-resolution method for subsurface target detection.

Three-dimensional (3D)-GPR is a new type of non-destructive detection equipment that can reconstruct underground 3D structure detection information. Compared with 2D-GPR, the 3D-GPR array antenna is able to acquire huge amounts of seamlessly stitched radar data without resulting in a lack of subsurface information. The 3D array antenna realizes true 3D acquisition, which makes the underground target imaging clear and

accurate, and can display any depth horizontal slice of the underground target [1]. There are now many commercially available 3D-GPR devices, and the scope and capabilities of the technology are gradually evolving. GPR has also been successfully used to provide forensic information during criminal investigations [2,3], to detect buried mines [4–6], to survey roads [7–9], to detect utilities [10,11], to measure geophysical strata [12–14], and in other areas [15,16].

The 3D GPR data have high requirements for positioning accuracy because of the high sampling density. Large positioning errors may cause distortion of GPR data, as in Figure 1a. Only 3D GPR systems with centimeter-level positioning accuracy can collect high-quality 3D GPR data. In addition, with regard to the surface area required to perform covered underground detection, due to the limited single detection width of the 3D GPR system, it is usually necessary to operate in strips, and the positioning accuracy of 3D GPR directly affects the position alignment effect between channels and strips, as shown in Figure 1b, which in turn affects the data quality of underground remote sensing detection. Thus, 3D GPR positioning affects the quality and accuracy of underground remote sensing detection data. Therefore, the accurate positioning of the GPR system is crucial.

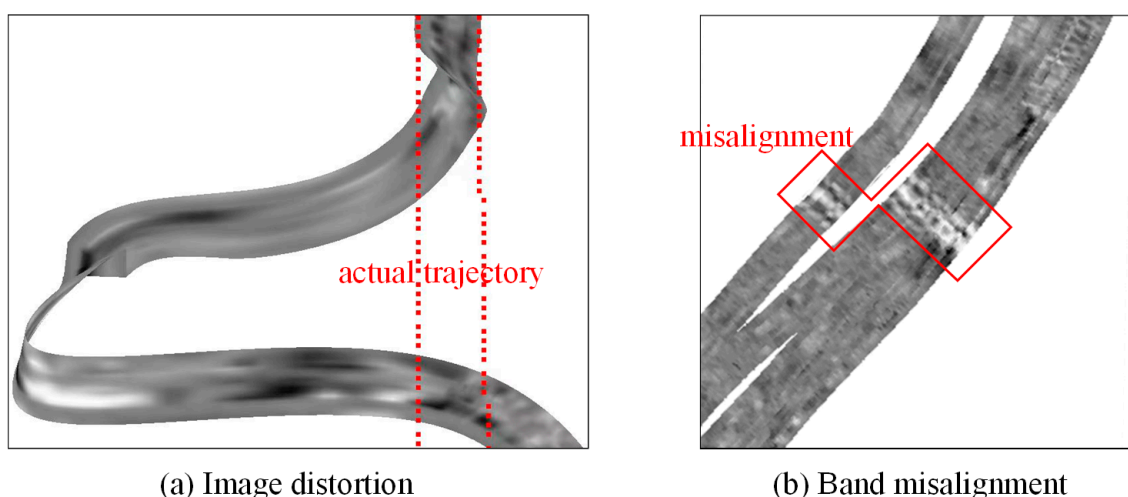


Figure 1. Results due to 3D GPR positioning errors.

The 3D-GPR positioning is generally achieved by laying out acquisition grids in the early stages [17,18], and the positioning accuracy is improved by modifying the encoder [19]. These methods have significant limitations, as the measurement needs to be kept straight. In addition, since no height information is available, the ground should not have too much undulation, and the measurement area should be smooth in topography. The positioning method without recording elevation information is obviously not suitable for 3D GPR, which requires x , y , and z coordinates.

Later, with the development of survey technology, various positioning techniques began to be used to improve 3D GPR positioning accuracy. At present, 3D GPR mainly uses GNSS for positioning. However, the positioning accuracy is affected by the quality of satellite signals. In practical applications, 3D GPR is used to survey a variety of environments, including roads, woods, and other areas surrounded by tall buildings or trees. These areas experience difficulty in receiving a sufficient number of satellite signals. The positioning accuracy of the 3D GPR system cannot be guaranteed simply by using a GNSS solution, and thus the quality of 3D GPR data cannot be guaranteed. In the environment with no satellite signals, such as tunnels or underground mines, these devices have no access to position information, which in turn does not allow for a reconstruction of the 3D underground space.

In addition, self-tracking systems, such as self-tracking robotic terrestrial positioning systems (TPSs) [20] and self-tracking total stations (TTSs) [21,22], were introduced in ground-penetrating radar positioning. These can achieve centimeter-level positioning accuracy. But, in dense urban areas, the signal tracked by the self-tracking system is lost when a clear line of sight is not available.

Other applications include the GPR positioning algorithm based on video recordings and special marker recognition [23], as well as a high-precision handheld GPR positioning system using an ultra-wideband (UWB) radio module [24]. In these positioning methods, with the help of RLPS and other mapping equipment and technology, positioning accuracy is significantly improved. However, these GPR data positioning methods need to set up one or more pieces of positioning equipment in the detection area and need to specify the detection route and delineate the detection range. When the ground is undulating and the shape of the detection area is irregular, one cannot lay positioning instruments in complex detection scenarios, limiting the possibility of flexible and convenient detection.

The Mobile Laser Scanner (MLS) has long been used in the field of land surveying. Studies [25,26] integrate MLSs into GPR. MLSs obtain ground point clouds of the ground that can be constructed in 3D space and correct the elevation of the GPR data. However, it is not possible to obtain accurate x , y coordinates. The portable rotary laser positioning system (RLPS) was applied to the GPR real-time positioning solution by Grasmueck and Viggiano [27]; this could obtain accurate centimeter-level x , y , and z coordinates. These positioning methods are aimed at small-scale underground detection, requiring GPR acquisition instruments in the range that other positioning equipment can capture, so they are not suitable for a large range of underground detection tasks, such as kilometer-level roadbed detection, large areas of underground pipeline detection, and other tasks.

There have also been some studies [28–30] that used SLAM algorithms to assist in GPR positioning. They integrated existing commercial mobile measurement systems with GPR and used SLAM algorithms to accomplish positioning in areas where GNSS signals were not available. However, the SLAM algorithm was not targeted to improve the GPR, which resulted in a GPR offset in the z -direction. In addition, some studies [29,30] do not add RTK GNSS, so if a survey area is wide and flat with no features, the laser scanner will not be able to obtain a valid point cloud to participate in the positioning. Moreover, in areas where GNSS signals are available, adding GNSS to participate in positioning can improve the positioning accuracy.

This paper proposes a high-precision positioning method with multi-level and multi-sensor fusion for 3D GPR integrated aboveground and underground remote sensing surveys. For the challenges of high-precision positioning of 3D GPR underground data and seamless splicing of multiple bands, an integrated aboveground and underground 3D mobile survey system is proposed and designed. It realizes the synchronous acquisition of an aboveground 3D laser point cloud, GNSS/IMU positioning and attitude, and underground 3D spatial data. The mobile survey module and the GPR control module were designed and developed with smaller hardware size, integrated acquisition and control, and more autonomy in solving the positioning data. Based on the multi-source data acquired by the system, a multi-level and multi-source data fusion positioning method is proposed for underground 3D GPR data. In areas without GNSS signals, this paper proposes a new and improved SLAM algorithm, which makes full use of the ground constraints through the double-threshold ground filtering algorithm and can effectively control the drift of the SLAM system in the z -direction. In areas with good GNSS signals, the tightly coupled GNSS/INS is used for positioning, and the positioning accuracy is higher compared with the SLAM algorithm. Through GNSS/INS tightly coupled positioning and laser SLAM positioning, this method realizes a positioning accuracy within 10 cm and a full spatial survey aboveground and underground, in an environment with or without good GNSS signals.

2. Materials and Methods

In order to enable 3D GPR to achieve multi-scene and multi-level high-precision positioning, an aboveground and underground integrated 3D mobile survey system is firstly designed. The GNSS receiver collects the GNSS signals for obtaining the position information of the system. The IMU acquires inertial data for obtaining the attitude and acceleration of the system. Attitude and acceleration from the inertial data are required for the GNSS/INS tightly coupled solution and SLAM algorithms. The 3D laser scanning system collects point cloud data for participating in SLAM positioning while constructing the 3D spatial structure on the ground. The 3D GPR acquires the underground 3D spatial data. In scenes with good GNSS signals, such as open squares, fast and high-precision positioning can be achieved based on GNSS data using differential GNSS technology. In scenes with weak GNSS signals, such as roads obscured by tall buildings or border trees, high-precision positioning of subsurface data can be achieved by using GNSS and IMU, combining position and attitude information, and using GNSS/INS tightly coupled solution technology. In scenes where GNSS signals are completely absent, such as tunnels and underground mines, SLAM technology is used for positioning based on INS data and 3D point cloud data. Ultimately, the underground data can be positioned with high precision in any scene, as shown in Figure 2.

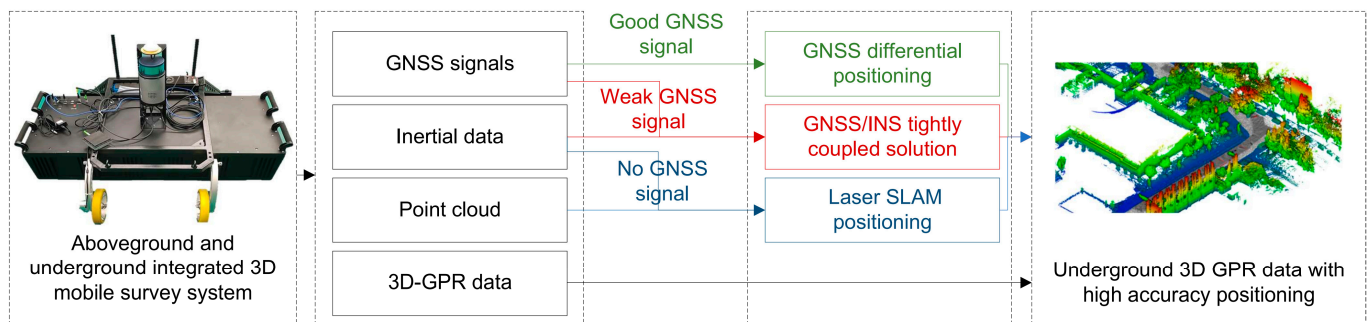


Figure 2. Multi-level and high-precision positioning of 3D GPR underground remote sensing detection.

In terms of hardware, the aboveground and underground integrated 3D mobile survey system is equipped with a GNSS receiver module, an inertial measurement unit module (IMU), a 3D laser scanner, and a 3D GPR. A GNSS receiver capable of receiving more than four satellites continuously can be characterized as being in an environment with good signals. With good GNSS signals, the combined positioning of GNSS and IMU can improve the positioning accuracy of 3D GPR. When the number of satellites is insufficient or even zero for a long time, the 3D LiDAR active positioning with the laser SLAM algorithm ensures 3D GPR positioning accuracy.

2.1. Aboveground and Underground Integrated 3D Mobile Survey System

The aboveground and underground integrated 3D survey system designed in this paper consists of a 3D mobile survey system and a GPR system. The GPR system explores the subsurface, and the 3D mobile survey system is used to locate the GPR and acquire the ground point cloud data. The configuration of the aboveground and underground integrated 3D survey system is shown in Figure 3. A cart is used as a carrier platform, where the 3D mobile survey system is mounted on the GPR system to obtain high-precision positioning information and ground point cloud data while the GPR obtains subsurface data. Figure 4 shows a simplified layout of the 3D survey system. The control units of the 3D mobile survey system and the GPR system are connected via an ethernet cable to the control PC, which controls both areas of data acquisition using the operating software.

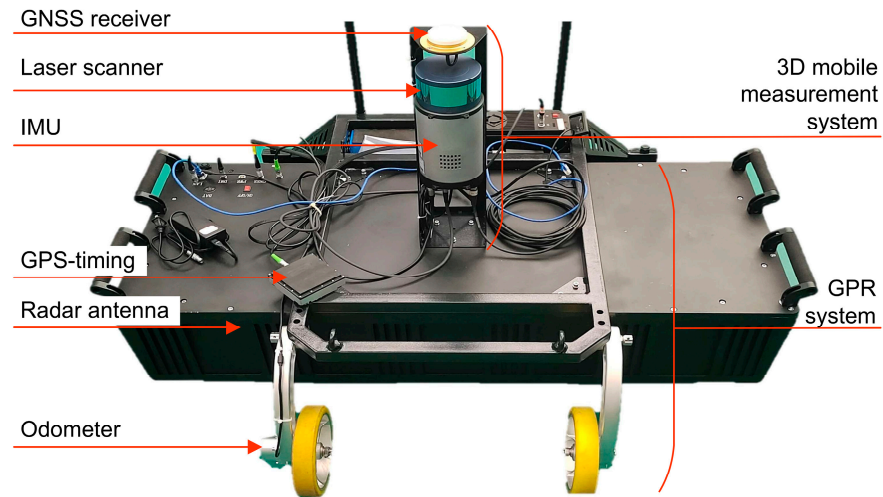


Figure 3. Aboveground and underground integrated 3D survey system configuration.

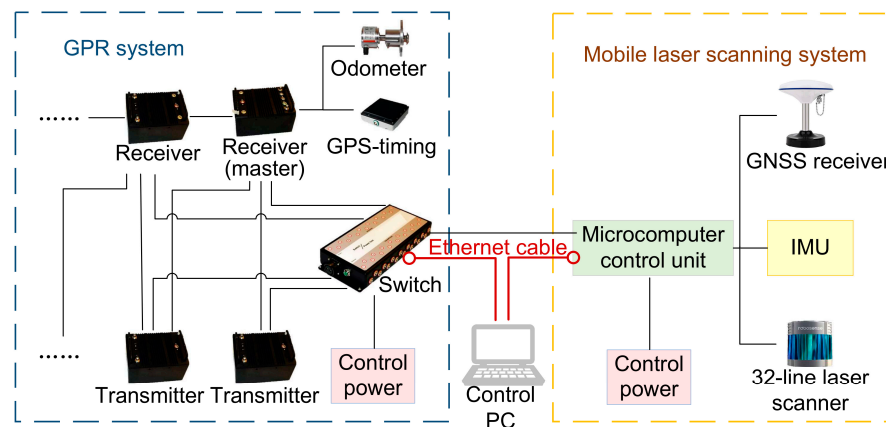


Figure 4. Simplified system layout with the aboveground and underground integrated 3D survey system.

2.2. Multilevel Positioning Framework

The aboveground and underground integrated 3D survey system gives the position attitude information of 3D laser scanning mobile survey system to 3D GPR system through GNSS time synchronization to realize the high-precision positioning of 3D GPR underground remote sensing detection. The positioning process of the multi-level multi-sensor fusion is shown in Figure 5.

The aboveground and underground integrated 3D survey system collects GNSS signal data, INS inertial data, and laser point cloud data, based on which a multi-level ground-penetrating radar remote sensing detection and positioning method applicable to different measurement environments can be realized. In scenarios with good GNSS signals but still having some time GNSS data missing (such as general urban roads), the positioning information is obtained by a tightly coupled GNSS + INS solution, which can not only overcome the transient GNSS signals being missing but also obtain smoother and more accurate attitude trajectory information. In the measurement environment where GNSS signals are weak or GNSS is completely unavailable (e.g., in tunnels, under buildings), the combination of laser scanner + INS inertial unit is used to realize the system self-positioning by using laser SLAM technology, which does not rely on GNSS for operation and greatly improves the system's applicability. In summary, the multi-level ground-penetrating radar remote sensing detection and positioning method can ensure that the aboveground and belowground integrated 3D survey system in this paper has the capability of system positioning and 3D mine detection mapping applicable in any environment.

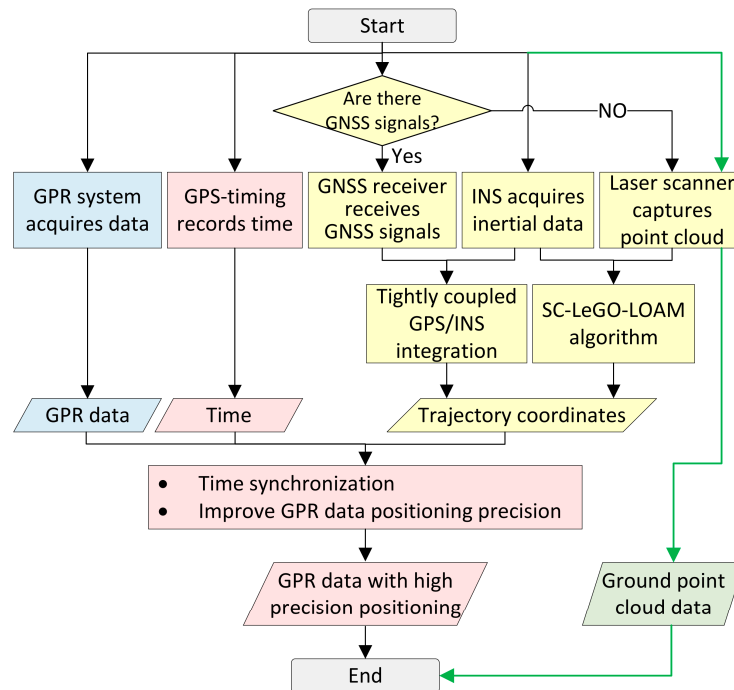


Figure 5. Flow chart of GPR data acquisition and positioning processing.

2.2.1. GNSS Differential Positioning with Good GNSS Signals

The GPR system is equipped with GNSS receivers; when the GNSS signal quality is good, fast positioning can occur based on the signal received from the GNSS receiver using the GNSS differential technique, as shown in Figure 6. GNSS differential technology is a method that can effectively reduce measurement errors to improve positioning accuracy. The measurements of satellite signals received by GNSS receivers all contain a certain amount of error, and some of these error terms are correlated in time and space, which is the fundamental reason for being able to use GNSS differential technology.



Figure 6. GNSS differential positioning in scene with good GNSS signals.

The deployment of additional reference stations is required to use differential technology, which is different from GNSS receivers. In addition to tracking visible satellite signals, the reference station has the function of transmitting signals. At a certain moment, the position coordinates of the reference station are precisely known, so its distance to the satellite is also precisely known. The reference station also measures the pseudo-range carrier phase measurements at this time. The difference value between the measured value and the actual value is the measurement error at the reference station at the current moment. The reference station continuously sends out the calculated measurement errors. The GNSS

receivers within its signal coverage area can correct the measured pseudo-range carrier phase measurements. Positioning errors are reduced with the help of received differential corrections. The closer the distance to the reference station, the higher the correlation between the measurement errors and the better the effect of differential positioning.

2.2.2. GNSS/INS Tightly Coupled Positioning with Weak GNSS Signals

The pure GNSS differential algorithm positioning method has a simple workflow and is easy to implement, but it has a low positioning density and relatively low accuracy and is also completely dependent on the quality of the GNSS signals. Once the GNSS receiver is blocked or jammed, the GNSS signals will experience loss of lock, and thus the complete positioning cannot be achieved. However, GPR detection environments are complex and diverse; for example, detection on roads may be blocked by tall buildings and border trees on both sides of the road, detection in woods may be blocked by the dense tree canopy, and detection in tunnels may not even receive GNSS signals at all. In order to locate and increase the positioning accuracy even when the GNSS signals are weak or are out of lock in the short term, this paper combines GNSS and INS by using a tightly coupled GNSS/INS solution based on the pseudo range and the pseudo-range rate for positioning, as shown in Figure 7.



Figure 7. GNSS/INS tightly coupled positioning in scene with weak GNSS signal.

The basic principle of the GNSS/INS tightly coupled solution positioning algorithm is as follows. The pseudo range and pseudo-range rate output from the GNSS receiver are used as the reference information for the combined GNSS/INS solution. The calculated pseudo range and pseudo-range rate between the carrier and the satellite are used as the measurement information for the combined GNSS/INS solution. In addition, the difference between the two is used as the observation information of the system. The error information of INS (misalignment angle, velocity error, position error) and the clock error information of GNSS receiver are estimated by Kalman filtering; then, the system is corrected by open-loop output or closed-loop feedback [20]. The flow chart of GNSS/INS tightly coupled positioning is shown in Figure 8.

The tightly coupled results are smoothed after the solution is finalized. When there are breakpoints in the positioning results, processing with the smoothing algorithm not only reduces position, velocity, and attitude errors caused by GNSS signals' loss of lock, but also smooths the trajectory. GNSS/INS tight coupling can output high-update rate position

information due to the INS output frequency of 500 Hz. The tight coupling provides continuous, high-accuracy, high-update rates and smooth positioning results, even when the GNSS receiver is tracking less than four satellites.

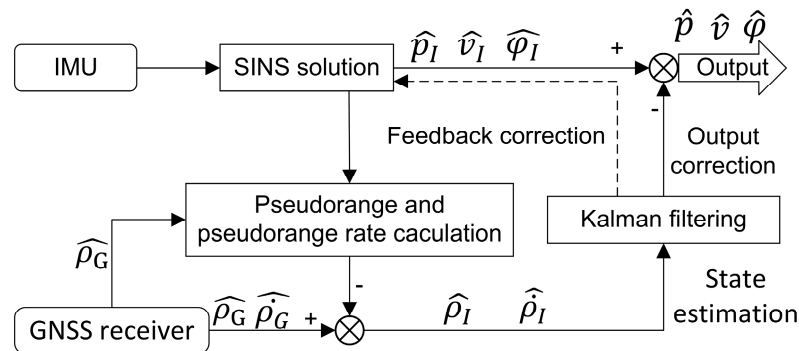


Figure 8. Flow chart of GNSS/INS tightly coupled positioning.

2.2.3. Laser SLAM Positioning with No GNSS Signal

Lidar is used for autonomous positioning in environments where GNSS signals are out of lock for a long time or even where there is no signal. In this paper, we use the tightly coupled iterative Kalman filter of FAST-LIO and FAST-LIO2 to implement the laser odometry module. Based on ScanContext [21] and LegoLOAM [22], we add Scan Context loopback detection to achieve the mapping optimization module.

Laser odometry high-frequency real-time operation is used to track the real-time motion. Forward propagation is performed for IMU pre-integration to obtain the prediction state and prediction error. The point cloud after ground segmentation is motion-compensated by backward propagation to obtain an in-frame distortion-free point cloud. The point-to-face distance is calculated as the residual, and the state is updated by iterative Kalman filtering until convergence, when the odometer is output.

The mapping optimization low frequency operates for closed-loop detection and optimization. The odometer estimated by the state estimation module will be added to a factor map in the form of factors; also introduced are the closed-loop factors obtained by scan matching. The odometer information is used to provide constraints for adjacent scans to ensure the accuracy of local maps, and the closed-loop information is used to provide constraints for global maps to ensure that large-scale map building can be performed properly. The flow chart of laser SLAM positioning is shown in Figure 9.

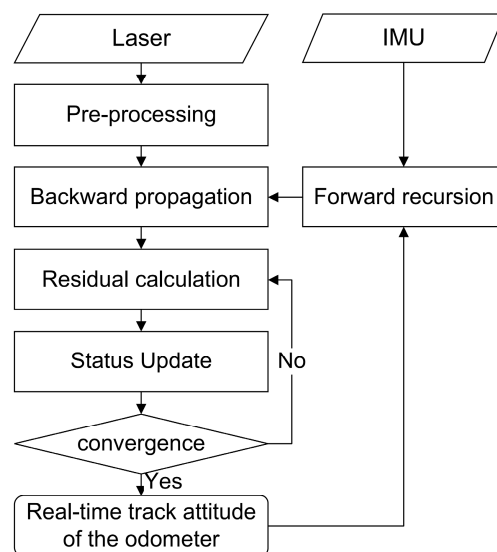


Figure 9. Flow chart of laser SLAM positioning processing.

Based on this framework for laser SLAM positioning, this paper improves the adaptability of adjacent frame matching and point cloud motion estimation in the framework.

1. Point cloud adjacency frame matching

In this paper, the ground point is filtered using a point cloud feature point matching method based on double-threshold ground filtering. The feature points are extracted by using a curvature-based point cloud feature extraction algorithm for non-ground points, and the feature points are aligned.

The specific algorithm steps are as follows.

Step 1: Double-threshold ground filtering process to filter out non-ground points

(1) Project p_{fk} onto the reference plane of the grid M . (2) Refine the roughly determined ground point G_{rough} as the determined ground point G using the RANSAC method. (3) Remove the NaN (Not a number) point cloud of non-ground point NG and points with too-close distance measurement results. The process is as in Algorithm 1.

Algorithm 1: Double-threshold ground filtering algorithm

Input: k moment point cloud $p_k^{(i)}$

Output: non-ground points NG

// Minimum distance $ring_{radius}$; Max distance $ghost_{radius}$; Height threshold $\delta h_1, \delta h_2$

While ($p_k^{(i)} \in p_k$) do

if $ring_{radius} * ring_{radius} < Distance < ghost_{radius} * ghost_{radius}$
 $p_k^{(i)} \in p_{fk}$

While ($p_{fk} \in M_i$) do

for ($p_{fk}^{(i)} \in p_{fk}$) do

if $h_k - h_{min}^{(i)} < \delta h_1$ and $h_{min}^{(i)} - h_{minmin}^{(i)} < \delta h_2$
 $p_{fk}^{(i)} \in G_{rough}$

if $p_k^{(i)} \notin G$

$p_k^{(i)} \in NG$

Step 2: Non-ground point cloud feature extraction based on curvature

Calculate the smoothness c of the Lidar points p_i in each frame of non-ground point NG for which curvature is to be found. Rank all the data according to the magnitude of the smoothness c . Classify the feature points into two categories, edge points ε_k and plane points H_k . Calculate using Equation (1).

$$c = \frac{1}{|S| \cdot \|X_{(k,i)}^L\|} \left\| \sum_{j \in S, j \neq i} (X_{(k,i)}^L - X_{(k,j)}^L) \right\| \quad (1)$$

where S in Equation (1) is the set of continuous points of i returned by the laser scanner in the same scan, and there is a point i in the coordinate system $\{L_k\}$ whose origin is located at the geometric center of the Lidar; $i \in p_k$ is the coordinate of a point in the point cloud sensed during scan k as $X_{(k,i)}^L$.

Edge points ε_k and face points H_k feature points are obtained within each scan line based on the edge point features with larger discrete curvature and face point features with smaller discrete curvature extracted from the discrete curvature of the single-frame Lidar point cloud.

Step 3: Feature matching based on edge points and face points

The point cloud p_k obtained during scan k is projected to the timestamp t_{k+1} to obtain \bar{P}_k . In the set ε_{k+1} of edge points in the feature points, the associated features of points are edges in \bar{P}_k . In the set H_{k+1} of plane points in the feature points, the associated features of

the points are plane blocks in \bar{P}_k . For edge points, their association features are lines, and for planar points, their association features are faces. The distances from the two types of feature points to their associated features are calculated separately, which will be used in the spatial 3D building section to estimate the motion of the Lidar.

2. Point cloud motion estimation

The motion attitude of the optical radar is calculated using the Lidar odometry method, and finally, the Lidar building module is used to refine the trajectory for 3D building to obtain an accurate trajectory and point cloud map. The specific steps are as follows.

Step 1: Lidar motion estimation

The set of edge and plane points, ε_{k+1} and H_{k+1} , obtained from p_{k+1} are obtained by curvature-based non-ground point cloud feature extraction, and $\tilde{\varepsilon}_{k+1}$ and \tilde{H}_{k+1} are the point sets projected to t_{k+1} . The transformation relationship between ε_{k+1} and $\tilde{\varepsilon}_{k+1}$ or H_{k+1} and \tilde{H}_{k+1} needs to be found to estimate the motion of the Lidar. Using $T_{k+1}^L = [t_x, t_y, t_z, \theta_x, \theta_y, \theta_z]^T$ to represent the motion attitude of the Lidar, Equation (2) can be derived.

$$X_{(k+1,i)}^L = R\tilde{X}_{(k+1,i)}^L + T_{(k+1,i)}^L(1:3) \quad (2)$$

where $X_{(k+1,i)}^L$ is the coordinate of point i in ε_{k+1} or H_{k+1} , $\tilde{X}_{(k+1,i)}^L$ is the coordinate of the corresponding point in $\tilde{\varepsilon}_{k+1}$ or \tilde{H}_{k+1} , $T_{(k+1,i)}^L(1:3)$ is the first to third set of $T_{(k+1,i)}^L$, and R is the rotation matrix defined by the Rodriguez formula.

Step 2: The motion attitude of the Lidar calculated by the Lidar odometry method

The input value of the Lidar mileage calculation method is the undistorted point cloud \bar{P}_k . The point cloud p_{k+1} is obtained during $k+1$, and the attitude T_{k+1}^L is obtained with respect to the Lidar odometer.

By the distances between the points in $\tilde{\varepsilon}_{k+1}$ and \tilde{H}_{k+1} and their associated features, the geometric relationship between the edge points in ε_{k+1} and the corresponding edge lines can be derived, as shown in Equation (3).

$$f\varepsilon(X_{(k+1,i)}^L, T_{k+1}^L) = d\varepsilon, i \in \varepsilon_{k+1} \quad (3)$$

Similarly, the geometric relationship between the points in H_{k+1} and their associated planar blocks is

$$fH(X_{(k+1,i)}^L, T_{k+1}^L) = dH, i \in H_{k+1} \quad (4)$$

Next, the Levenberg–Marquardt method is used to estimate the motion of the Lidar. For each feature point in ε_{k+1} and H_{k+1} using the derived Equations (3) and (4), a nonlinear function, such as specified in Equation (5), can be obtained.

$$f(T_{k+1}^L) = d \quad (5)$$

Equation (5) is solved by minimizing the distance between each feature point and its associated feature to zero in a nonlinear iteration, as shown in Equation (6).

$$T_{k+1}^L \leftarrow T_{k+1}^L - (J^T J + \lambda \text{diag}(J^T J))^{-1} J^T d \quad (6)$$

λ is a factor determined using the Levenberg–Marquardt method. Double-squared weights are assigned to each feature point in this process, and iterations are performed to update the motion pose T_{k+1}^L of the Lidar for nonlinear optimization until the end of the iteration; the results are input to the Lidar map building module for processing.

3. Results

3.1. Experiment Area and Data

3.1.1. Experiment with Good GNSS Signals

The orthophoto of the measurement area of the experiment in the good GNSS environment is shown in Figure 10. The experiment was conducted at Wuhan University, where we surveyed the underground area of Zhuoer Gymnasium Ring Road, with a measured length of 872 m. The road was wide, with no trees or tall buildings blocking the road on both sides, and the GNSS signal quality was good. The number of satellites tracked by the GNSS receiver in the survey area is shown in Figure 11. Only in the middle few seconds of the time is the number of tracked satellites less than 4; the other moments have good satellite observation. We placed 13 metal plates of 35 cm × 35 cm on the road as positioning targets in order to calculate the system positioning accuracy.

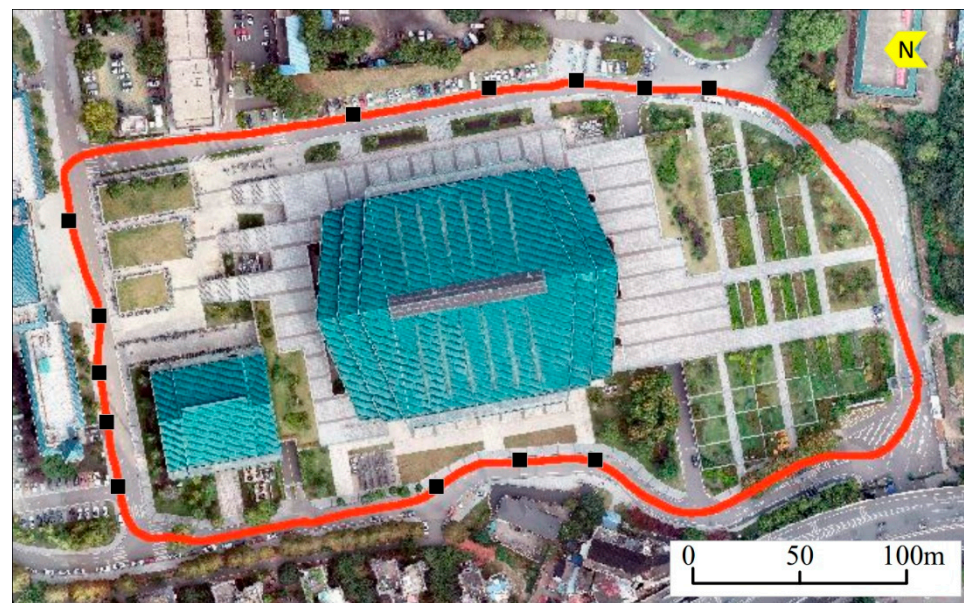


Figure 10. DOM, measurement trajectory and positioning target distribution of the good GNSS environment.

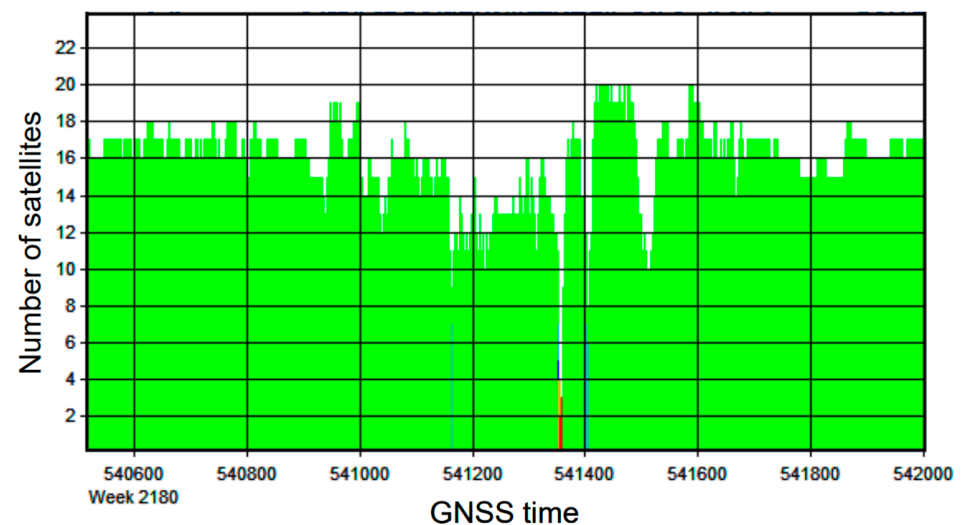


Figure 11. Number of satellites tracked by GNSS receivers in the good GNSS environment.

3.1.2. Experiment with Weak GNSS Signals

The orthophoto of the measurement area of the experiment in the partly loss-of-lock GNSS environment is shown in Figure 12. The experiment surveyed the underground area of the road around the playground of the Department of Informatics of Wuhan University; the length of the road is 630 m, the width of the road is about 5 m, the road is surrounded by dense trees and tall buildings and twice traverses the internal space of the building up to 20 m, and the environmental GNSS signals are seriously obscured. The number of satellites tracked by the GNSS receiver in the survey area is shown in Figure 13; excluding the good condition of GNSS satellites at the beginning and end of the static convergence phase of the measurement as well as the ability to track four satellites for part of the measurement process, there was an insufficient number of satellites or even zero satellites for a large part of the measurement time. As shown in Figure 12, 10 metal plates of 35 cm × 35 cm were evenly placed on the road as positioning targets to evaluate the positioning accuracy of the aboveground and underground integrated 3D survey system.



Figure 12. DOM, measurement trajectory, and positioning target distribution of the partly loss-of-lock GNSS environment.

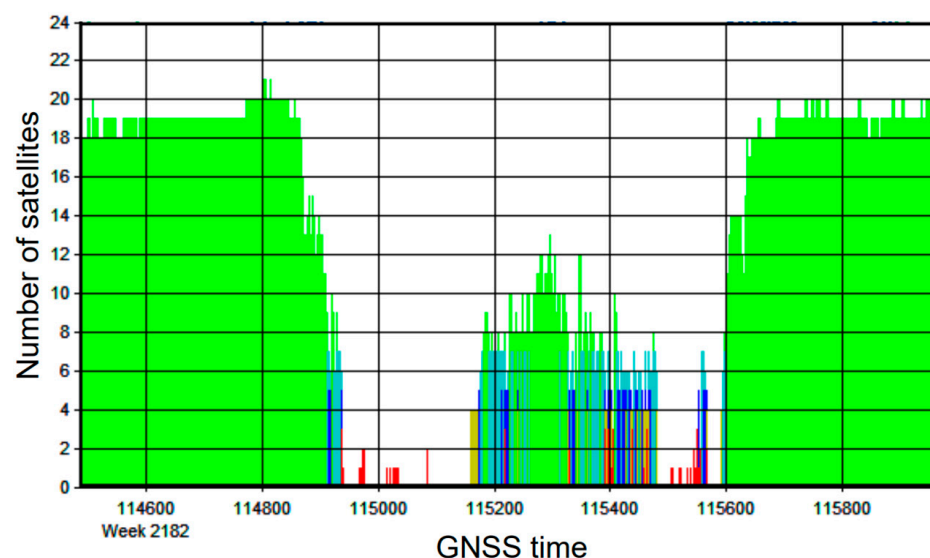


Figure 13. Number of satellites tracked by GNSS receivers in the partly loss-of-lock GNSS environment.

3.2. Positioning Results and Accuracy Analysis

3.2.1. Experiment with Good GNSS Signals

1. Trajectory results

As shown in Figure 14, the trajectory results of the GNSS differential solution, GNSS/INS tightly coupled solution, and laser SLAM autonomous positioning are obtained under the good GNSS signal environment. It can be seen that there are two interruptions in the trajectory of GNSS differential decomposition, while the trajectories of GNSS/INS tightly coupled decomposition and laser SLAM autonomous positioning are continuous, without interruption, and relatively smooth.

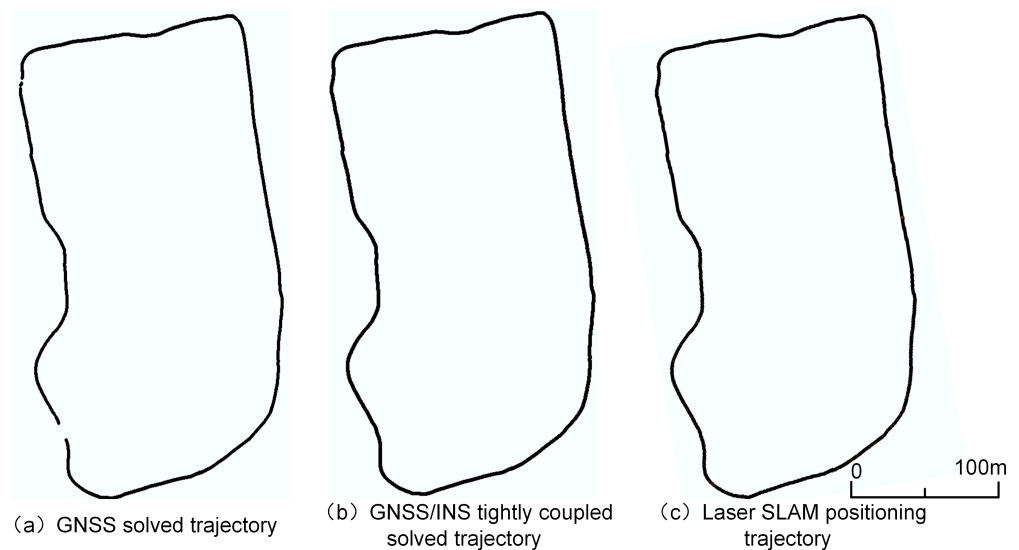


Figure 14. The results of solving the trajectory by three positioning methods in the GNSS good environment.

2. Positioning accuracy evaluation

The cart passed through 13 metal positioning targets during the measurement of experiment in the GNSS good environment. The coordinates of the center points of the targets can be calculated and extracted from each of the three positioning methods: the GNSS differential positioning corresponding to imaging, GNSS/INS tightly coupled positioning corresponding to imaging, and laser SLAM autonomous positioning. It is possible to count the errors between the coordinates and the true values at the 13 control points for the three positioning methods. Table 1 shows the statistics of positioning precision of the three positioning strategies for the experiment in the GNSS good environment at the 13 control points.

Table 1. Statistics of positioning precision of three positioning strategies for the GNSS good environment.

| Methodology | Direction | MIN (m) | MAX (m) | AVE (m) | S.D. | RMSE (m) |
|-------------|-----------|---------|---------|---------|-------|----------|
| GNSS | E | 0.007 | 0.222 | 0.067 | 0.077 | 0.099 |
| | N | 0.003 | 0.107 | 0.036 | 0.037 | 0.050 |
| GNSS/IMU | E | 0.001 | 0.043 | 0.014 | 0.012 | 0.018 |
| | N | 0.000 | 0.066 | 0.014 | 0.018 | 0.022 |
| SLAM | E | 0.001 | 0.112 | 0.054 | 0.038 | 0.057 |
| | N | 0.000 | 0.087 | 0.032 | 0.028 | 0.037 |

From Table 1, it can be seen that the highest positioning accuracy is achieved by the GNSS/INS tightly coupled decomposition positioning method, with the average positioning error being less than 0.01 m in both the east and north directions and the RMSE

around 0.02 m, and the minimum, maximum, mean, standard deviation and RMSE of the errors all at a minimum. Only the GNSS differential decomposition algorithm positioning method and the laser SLAM self-localization method performed comparably, with the mean error and RMSE higher than 0.05 m in the east direction. The experiment in the GNSS good environment shows that the system can obtain the best positioning effect by using the GNSS/INS tightly coupled decomposition positioning method in the case of good GNSS signals.

The GNSS positioning frequency is about 1–10 hz, and the IMU sampling frequency in the system is up to 500 hz. The IMU does not lose information during high-speed sampling, which can improve the sampling and positioning accuracy. It can also obtain high-precision attitude information for correcting the positioning attitude. With the combined GNSS/INS tightly coupled positioning, even if there is a short time quality degradation of the GNSS signals, the high-precision IMU can still provide continuous high-precision position reference. As a result, the positioning accuracy is not affected.

3.2.2. Experiment with Weak GNSS Signals

1. Trajectory results

Figure 15 shows the trajectory results of GNSS differential decomposition, GNSS/INS tightly coupled decomposition, and laser SLAM autonomous positioning under the weak GNSS signal environment. The trajectory calculated by GNSS differential decomposition has good trajectory quality, except for the southernmost and northernmost ends, and the reliable GNSS signals cannot be tracked on the east, west, and south sides of the playground because of thick trees and building obstruction. Because GNSS has a long, uninterrupted out-of-lock period (the first out-of-lock time is about 3 min, and the second out-of-lock time is about 2 min), the trajectory has a wide range of interruptions, and it is basically impossible to determine the results. In contrast, the GNSS/INS tightly coupled solution can provide a short-term continuous high-accuracy position reference without affecting the positioning accuracy, even if the quality of GNSS signals is degraded for a short period of time due to the participation of INS in the calculation; the solved trajectory is continuous without interruption and with high solution accuracy.

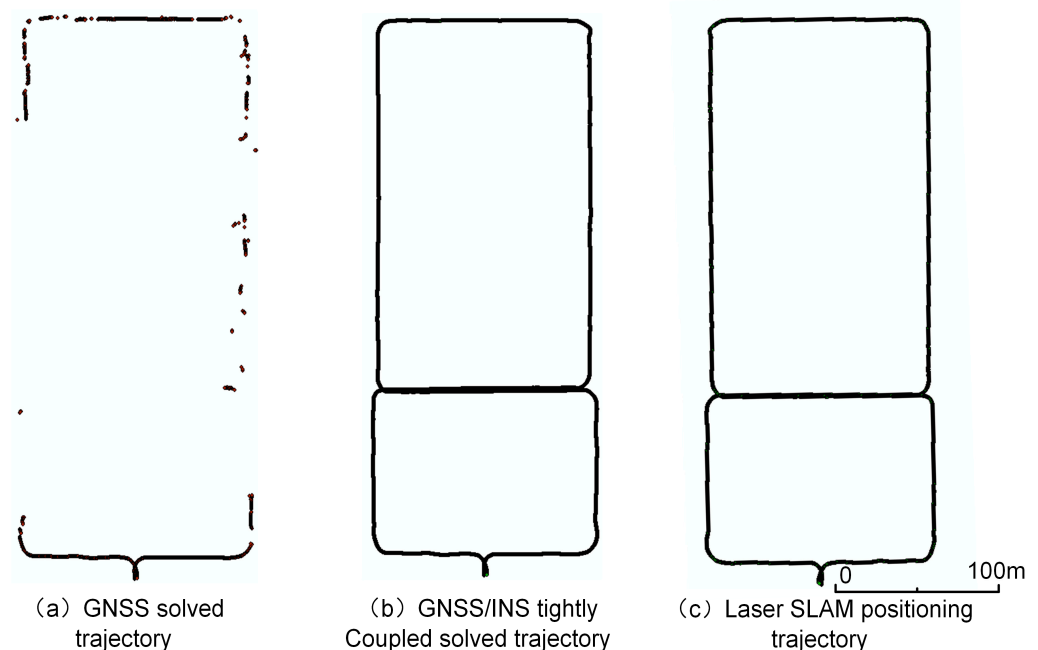


Figure 15. The results of solving the trajectory by three positioning methods in the GNSS partly loss-of-lock environment.

2. Positioning accuracy evaluation

The coordinates of the center point of the target can be calculated and extracted from the three positioning methods to obtain the coordinates of the 10 points. The positioning coordinates of the three positioning methods at the 10 control points were calculated, as was the error between them and the real values. Statistical analysis of the positioning errors was carried out; see Table 2.

Table 2. Statistics of positioning precision of different positioning strategies for the GNSS partly loss-of-lock environment.

| Methodology | Direction | MIN (m) | MAX (m) | AVE (m) | S.D. | RMSE (m) |
|-------------|-----------|---------|---------|---------|-------|----------|
| GNSS | E | 0.033 | 20.531 | 2.325 | 6.400 | 6.502 |
| | N | 0.013 | 3.530 | 0.710 | 1.041 | 1.216 |
| GNSS/IMU | E | 0.002 | 0.282 | 0.059 | 0.086 | 0.101 |
| | N | 0.000 | 0.218 | 0.075 | 0.078 | 0.105 |
| SLAM | E | 0.004 | 0.104 | 0.071 | 0.036 | 0.079 |
| | N | 0.002 | 0.130 | 0.089 | 0.037 | 0.095 |

As can be seen from Table 2, the accuracy of using pure GNSS positioning is very poor in scenarios where GNSS signals are weak or even absent. The maximum value of the error in the north direction is greater than 3 m, the average error value is 0.7 m, the RMSE is greater than 1 m, and the standard deviation of the error is greater than 1. The error fluctuation is large. The positioning accuracy of the east direction is slightly higher, while the error average and RMSE are tens of centimeters, and the accuracy is lower than that of the GNSS/INS combined positioning and SLAM positioning algorithms.

The difference in positioning accuracy between the GNSS/INS post-solution method and the SLAM algorithm is not significant. The RMSEs of the GNSS/INS combined positioning method are slightly greater than 10 cm for the east and north directions, while the RMSEs of the SLAM algorithm are less than 10 cm for both the east and north directions. The error standard deviation of SLAM shows smaller error fluctuations, and the maximum value of the error is smaller than that of the combined GNSS/INS positioning. GNSS signals are not used in the SLAM algorithm, so an accuracy better than 10 cm can be obtained using the laser SLAM positioning algorithm, whether or not GNSS signals are available.

3.3. 3D GPR Imaging Results

3.3.1. Experiment with Good GNSS Signals

Figure 16I shows an example of 3D GPR data positioning imaging in a good GNSS signal environment. The 3D GPR data represent a horizontal section located at 0.2 m below ground level. Figure 16II shows the local enlargements of the imaging corresponding to the GNSS differential positioning, the imaging corresponding to the GNSS/INS tightly coupled positioning, and the imaging corresponding to the laser SLAM autonomous positioning in the overall image.

Because of the good quality of GNSS signals in the environment, the overall shapes of the subsurface GPR data imaged based on the three positioning methods were basically the same, and no obvious deformation occurred. Comparing with the local zoomed-in figure (Figure 11), the GPR data based on GNSS differential decomposition localization showed trajectory jitter or slight deformation in individual areas, as in part (a), (b), and (e) of the figure. In contrast, the GPR data based on GNSS/INS tightly coupled decomposition and laser SLAM self-localization have smooth trajectories throughout, and no deformation phenomenon occurs.

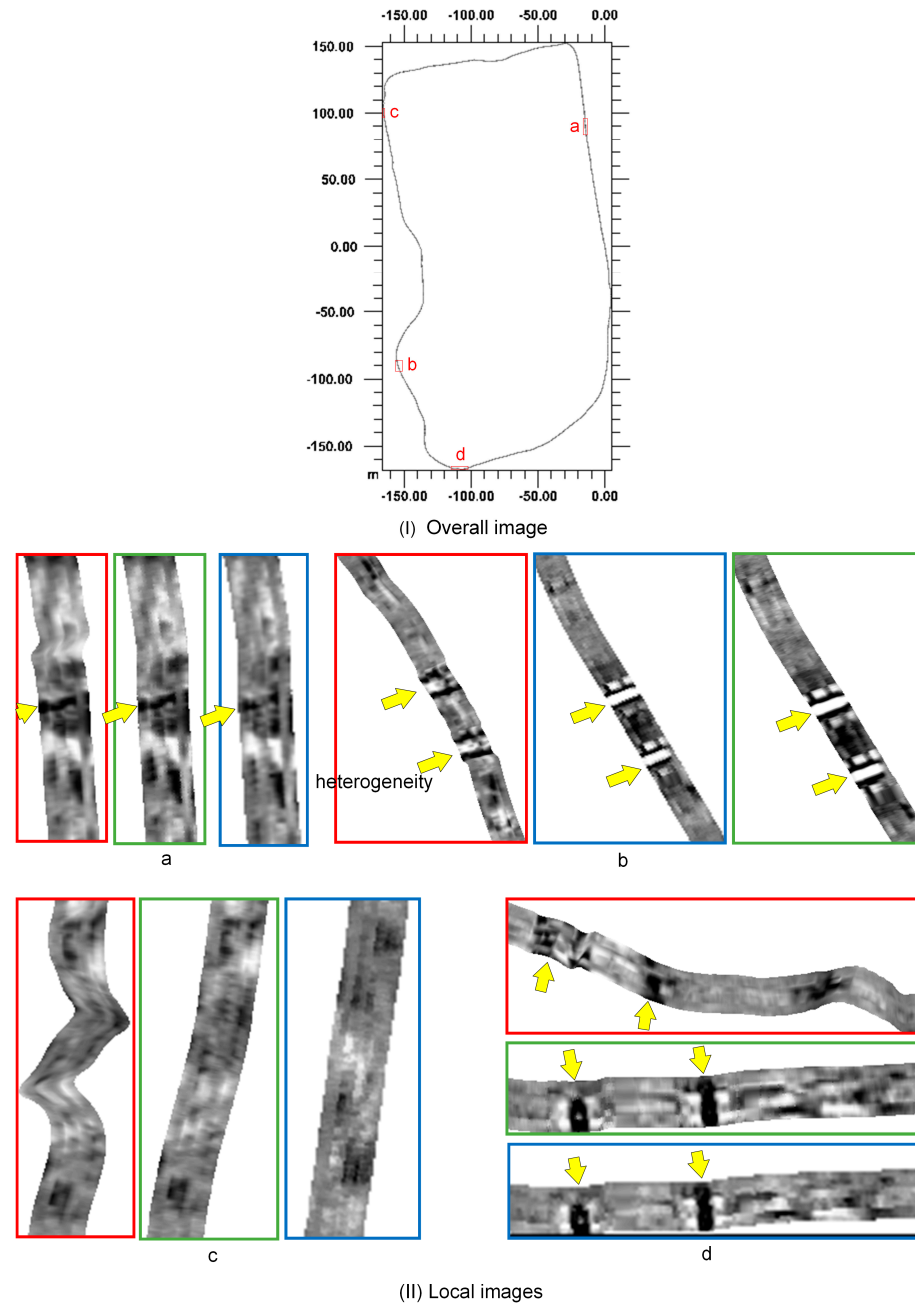


Figure 16. Overall and local images (horizontal section) of 3D GPR data imaged by different positioning methods in the GNSS good environment, with local enlarged images of GNSS differential positioning (red border), GNSS/INS tightly coupled positioning (green border), and laser SLAM autonomous positioning (blue border). The local images respectively belong to regions a, b, c, and d of the overall image. (The yellow arrows point to heterogeneity).

3.3.2. Experiment with Weak GNSS Signals

Figure 17 shows an example of 3D GPR data positioning imaging in the GNSS partly loss-of-lock environment, in which the 3D GPR data are located at 0.2 m below the ground level in the horizontal section. In the experiment, except for the north and south ends, which receive a small number of satellite signals, the region receives less than four satellites and even zero satellites. GPR data based on GNSS differential decomposition positioning as a whole have a dramatic deformation and serious track drift; thus, GPR data cannot be imaged properly. The overall shapes of subsurface GPR data imaging based on GNSS/INS tightly coupled decomposition and laser SLAM-based self-localization methods are basically the same.

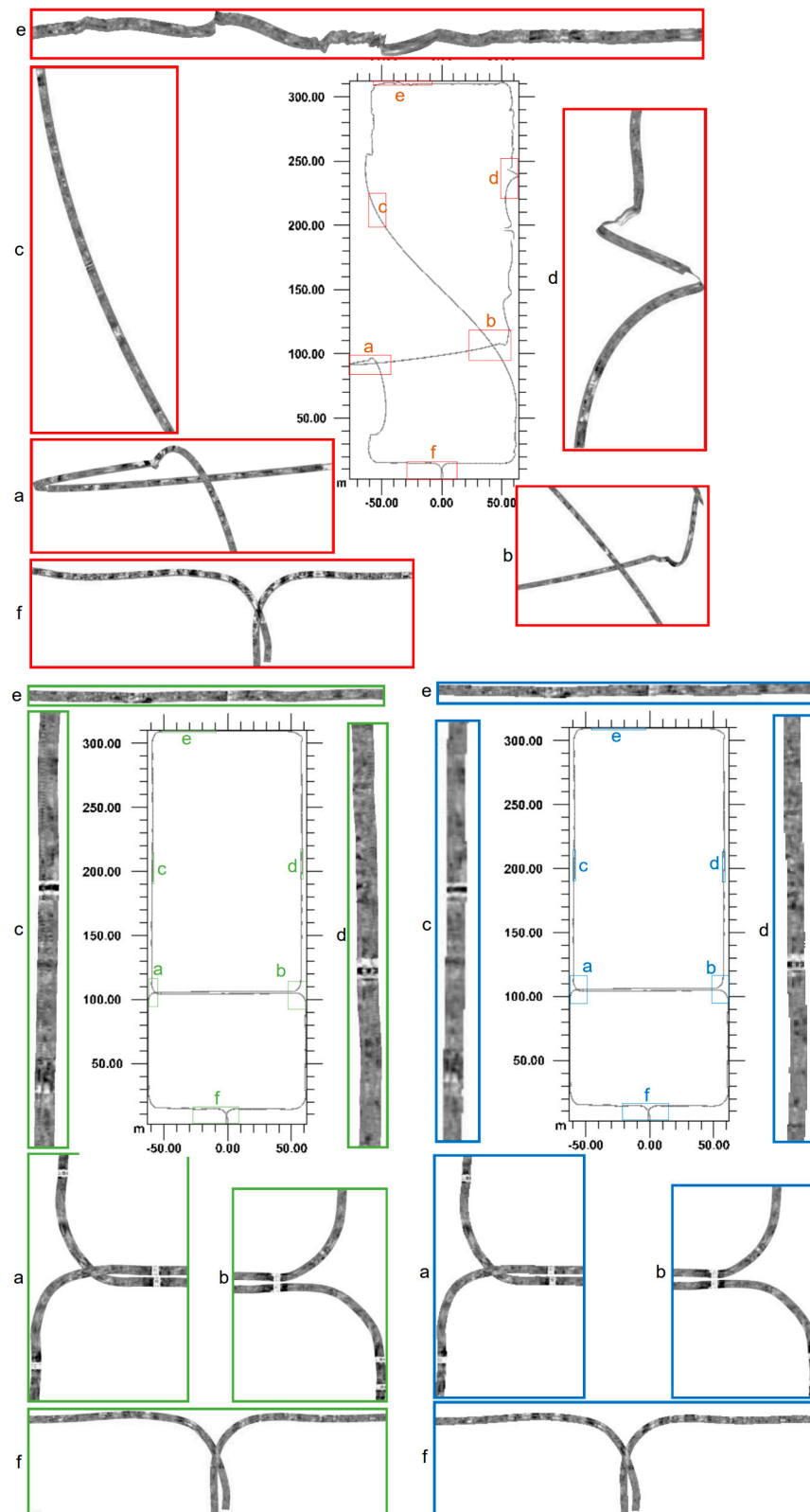


Figure 17. Overall and local images (horizontal section) of 3D GPR data imaged by different positioning methods in the GNSS partly loss-of-lock environment; GNSS differential positioning corresponding to 3D GPR image (red border), GNSS/INS tightly coupled positioning corresponding to 3D GPR image (green border), and laser SLAM autonomous positioning corresponding to 3D GPR image (blue border) in a locally enlarged view. The local images respectively belong to regions a, b, c, and d of the overall image.

Figure 17 shows the local enlargements of the imaging corresponding to GNSS differential positioning, GNSS/INS tightly coupled positioning, and laser SLAM autonomous positioning. From the local view, the subsurface GPR data based on GNSS/INS tight-coupling solution and laser SLAM-based autocalization methods show no obvious deformation in each part, and normal data interpretation and decoding can be performed.

4. Discussion

This paper proposes a 3D GPR positioning method based on a GNSS differential solution, GNSS/INS tightly coupled solution and LiDAR SLAM method, and proves the accuracy and effectiveness of the algorithm through underground detection tests in different scenes. Compared with the traditional positioning by GNSS only, we add the GNSS/INS tightly coupling algorithm and SLAM algorithm to cope with different survey environments. We carry out good and weak GNSS signal experiments and compare the positioning accuracy using the GNSS algorithm, GNSS/INS tightly coupled algorithm, and SLAM algorithm. It is demonstrated that this multi-level positioning method has high accuracy and good robustness.

In scenes with good GNSS signals, the 3D GPR positioning can be achieved quickly by using the GNSS differential solution method, and positioning accuracy within 10 cm can be achieved. Compared with the GNSS differential solution, the GNSS/INS tightly coupled solution is more complicated, but the positioning accuracy is significantly improved. Therefore, in a scene with good GNSS signals, 3D GPR should choose the GNSS differential solution for fast positioning and the GNSS/INS tight coupling solution for high positioning accuracy. The SLAM method has no obvious advantage at this time.

In the condition of weak GNSS signals, the positioning will be offset by using the GNSS differential solution method, while using the GNSS/INS tightly coupled solution method can still provide reliable positioning. The GNSS positioning frequency is about 1–10 Hz, while the sampling frequency of IMU in the aboveground and underground integrated 3D survey system is up to 500 Hz, which can improve the sampling and positioning accuracy without losing information in the high-speed sampling process. The addition of IMU can also obtain high-precision attitude information for correcting the positioning attitude. With the combined GNSS/INS positioning method, even if the GNSS signals have a quality degradation problem in a short period of time, the high-precision IMU can still provide a continuous high-precision position reference in a short period of time without affecting the positioning accuracy.

In the case where GNSS signals demonstrate loss of lock for a long time or no GNSS signals, the GNSS receiver cannot receive GNSS signals, and neither the GNSS differential solution nor the GNSS/INS tightly coupled solution can achieve positioning. Aboveground and underground integrated 3D mobile survey systems use Lidar, IMU, and odometers for positioning by laser the SLAM algorithm. The IMU obtains the prediction state and prediction error, and the motion compensation of the point cloud acquired by the Lidar obtains a distortion-free point cloud. The odometer is calculated and output, and the mapping is optimized to achieve closed-loop detection. The odometer information is used to provide constraints for adjacent scans to ensure the accuracy of local positioning, and the closed-loop information is used to provide constraints for global maps to ensure that large-scale positioning can be completed. Adjacent frame matching and point cloud motion estimation are adaptively improved to achieve high-precision autonomous positioning by laser SLAM. The laser SLAM autonomous positioning algorithm can obtain positioning results with an accuracy better than 10 cm. The SLAM method combines IMU and laser point cloud features at the level of primary observations, realizes joint nonlinear optimization of multi-source data, and achieves accurate positioning optimization using laser point cloud precision matching [31–33]. This enables this aboveground and underground integrated 3D survey system to acquire 3D underground medium distribution data with high-precision positioning information in environments without GNSS signals (e.g., underground mines and tunnels).

5. Conclusions

This paper proposed a high-precision positioning method of multi-level and multi-sensor fusion for 3D GPR aboveground and underground integrated detection. Through the designed aboveground and underground integrated 3D survey system, the underground medium distribution is detected, and the aboveground 3D spatial structure is measured at the same time, to realize the rapid integrated measurement of aboveground and underground space. The survey system is able to achieve high-precision positioning of 3D GPR in environments with or without GNSS signals.

Compared with GNSS solved positioning, in the case of good GNSS signals, the aboveground and underground integrated 3D survey system collects INS data, has higher sampling frequency and accurate attitude information, has more accurate positioning, and can be applied to high-speed measurement scenarios. In scenarios where GNSS signals are weak or interrupted, the system is able to ensure continuous positioning output due to the use of a tightly coupled GNSS and INS solver positioning method. Such environments are the main working scenarios of GPR systems and include roads, bridges, and woods; these contribute to the stable and reliable use of 3D GPR. In scenarios without GNSS signals, the system uses Lidar sensors for active positioning, and the experiments prove that the positioning accuracy is better than 10 cm, which means the 3D GPR can be used for underground mine safety inspection, long tunnel construction detection, etc. In addition, the point cloud data obtained by the laser scanner in the system can generate the 3D spatial structure of the ground space. This multi-source data of the integrated spatial structure above and below ground is useful for spatial display, comprehensive analysis, and decision making.

In conclusion, the aboveground and underground integrated 3D detection multi-level, multi-sensor fusion high-precision positioning method proposed in this paper can achieve integrated aboveground and underground rapid measurement in any environment and ensure better than 10 cm positioning accuracy, ensuring that the 3D GPR can complete accurate detection and large-scale survey and can provide data security for imaging and interpretation of underground data.

Author Contributions: Conceptualization, J.Z. and Q.H.; methodology, J.Z. and Q.H.; software, X.D.; validation, J.Z.; formal analysis, J.Z.; investigation, J.Z.; resources, J.Z.; data curation, J.Z.; writing—original draft preparation, J.Z.; writing—review and editing, J.Z. and Q.H.; visualization, J.Z.; supervision, P.Z.; project administration, Y.Z.; funding acquisition, Y.Z. and P.Z. All authors have read and agreed to the published version of the manuscript.

Funding: This research was funded by the Knowledge Innovation Program of Wuhan—Basic Research, grant number 2022010801010431; the Open Foundation of the Key Laboratory of National Geographic Census and Monitoring, Ministry of Natural Resources, grant number 2023NGCM08.

Data Availability Statement: The raw data supporting the conclusions of this article will be made available by the authors on request.

Conflicts of Interest: The authors declare no conflicts of interest. The funders had no role in the design of the study; in the collection, analyses, or interpretation of data; in the writing of the manuscript; or in the decision to publish the results.

References

1. Grasmueck, M.; Weger, R.; Horstmeyer, H. Full-resolution 3D GPR imaging. *Geophysics* **2005**, *70*, K12–K19. [[CrossRef](#)]
2. Novo, A.; Lorenzo, H.; Rial, F.I.; Solla, M. 3D GPR in forensics: Finding a clandestine grave in a mountainous environment. *Forensic Sci. Int.* **2011**, *204*, 134–138. [[CrossRef](#)]
3. Kelly, T.; Angel, M.; O'Connor, D.; Huff, C.; Morris, L.; Wach, G. A novel approach to 3D modelling ground-penetrating radar (GPR) data—A case study of a cemetery and applications for criminal investigation. *Forensic Sci. Int.* **2021**, *325*, 110882. [[CrossRef](#)]
4. Sato, M.; Yokota, Y.; Takahashi, K.; Grasmueck, M. Landmine detection by 3D GPR system. In Proceedings of the Detection and Sensing of Mines, Explosive Objects, and Obscured Targets XVII, Baltimore, MD, USA, 23–27 April 2012; Volume 8357, p. 835710.
5. Klesk, P.; Kapruziak, M.; Olech, B. Statistical moments calculated via integral images in application to landmine detection from Ground Penetrating Radar 3D scans. *Pattern Anal. Appl.* **2018**, *21*, 671–684. [[CrossRef](#)]

6. Ebrahim, S.M.; Medhat, N.; Mansour, K.K.; Gaber, A. Examination of soil effect upon GPR detectability of landmine with different orientations. *NRIAG J. Astron. Geophys.* **2018**, *7*, 90–98. [[CrossRef](#)]
7. Lee, S.-H.; Jang, I.-H. A Study on the Underground Condition of Road Using 3D-GPR Exploration. *J. Korean Geoenviron. Soc.* **2019**, *20*, 49–58.
8. Kang, M.-S.; Kim, N.; Im, S.B.; Lee, J.-J.; An, Y.-K. 3D GPR image-based UcNet for enhancing underground cavity detectability. *Remote Sens.* **2019**, *11*, 2545. [[CrossRef](#)]
9. Liu, Z.; Wu, W.; Gu, X.; Li, S.; Wang, L.; Zhang, T. Application of Combining YOLO Models and 3D GPR Images in Road Detection and Maintenance. *Remote Sens.* **2021**, *13*, 1081. [[CrossRef](#)]
10. Emilsson, J.; Viberg, A.; Gustafsson, J.; Langton, M.; Friberg, J. Efficient State-of-Art HDR 3D GPR Compared to 2D Traditional Utility Investigations. In Proceedings of the NSG2020 26th European Meeting of Environmental and Engineering Geophysics; European Association of Geoscientists & Engineers, Online, 7–8 December 2020; Volume 2020, pp. 1–4.
11. Feng, J.; Yang, L.; Wang, H.; Song, Y.; Xiao, J. Gpr-based subsurface object detection and reconstruction using random motion and depthnet. In Proceedings of the 2020 IEEE International Conference on Robotics and Automation (ICRA), Paris, France, 31 May–31 August 2020; pp. 7035–7041.
12. Luo, G.; Cao, Y.; Xu, H.; Yang, G.; Wang, S.; Huang, Y.; Bai, Z. Research on typical soil physical properties in a mining area: Feasibility of three-dimensional ground penetrating radar detection. *Environ. Earth Sci.* **2021**, *80*, 92. [[CrossRef](#)]
13. Zajc, M.; Urbanc, J.; Pečan, U.; Glavan, M.; Pintar, M. Using 3D GPR for determining soil conditions in precision agriculture. In Proceedings of the 18th International Conference on Ground Penetrating Radar; Society of Exploration Geophysicists, Golden, CO, USA, 14–19 June 2020; pp. 291–294.
14. Ercoli, M.; Di Matteo, L.; Pauselli, C.; Mancinelli, P.; Frapiccini, S.; Talegalli, L.; Cannata, A. Integrated GPR and laboratory water content measures of sandy soils: From laboratory to field scale. *Constr. Build. Mater.* **2018**, *159*, 734–744. [[CrossRef](#)]
15. Gaballah, M.; Grasmueck, M.; Sato, M. Characterizing subsurface archaeological structures with full resolution 3D GPR at the early dynastic foundations of Saqqara Necropolis, Egypt. *Sens. Imaging* **2018**, *19*, 23. [[CrossRef](#)]
16. Ozkan-Okay, M.; Kadioglu, S.; Samet, R. Enhancement of 2D/3D GPR Data Imaging by the Proposed TAEF Technique: Displaying Archeological Remains under the Colonnade Road in Anavarza Ancient City, Adana, Turkey. In Proceedings of the Geoinformatics, European Association of Geoscientists & Engineers, Online, 11–14 May 2021; Volume 2021, pp. 1–7.
17. Pipan, M.; Baradello, L.; Forte, E.; Prizzon, A.; Finetti, I. 2-D and 3-D processing and interpretation of multi-fold ground penetrating radar data: A case history from an archaeological site. *J. Appl. Geophys.* **1999**, *41*, 271–292. [[CrossRef](#)]
18. McMechan, G.A.; Gaynor, G.C.; Szerbiak, R.B. Use of ground-penetrating radar for 3-D sedimentological characterization of clastic reservoir analogs. *Geophysics* **1997**, *62*, 786–796. [[CrossRef](#)]
19. Grasmueck, M. 3-D ground-penetrating radar applied to fracture imaging in gneiss. *Geophysics* **1996**, *61*, 1050–1064. [[CrossRef](#)]
20. Šarlah, N.; Podobnikar, T.; Ambrožič, T.; Mušič, B. Application of Kinematic GPR-TPS model with high 3D georeference accuracy for underground utility infrastructure mapping: A case study from urban sites in Celje, Slovenia. *Remote Sens.* **2020**, *12*, 1228. [[CrossRef](#)]
21. Boniger, U.; Tronicke, J. On the potential of kinematic GPR surveying using a self-tracking total station: Evaluating system crosstalk and latency. *IEEE Trans. Geosci. Remote Sens.* **2010**, *48*, 3792–3798. [[CrossRef](#)]
22. Trinks, I.; Johansson, B.; Gustafsson, J.; Emilsson, J.; Friberg, J.; Gustafsson, C.; Nissen, J.; Hinterleitner, A. Efficient, large-scale archaeological prospection using a true three-dimensional ground-penetrating radar array system. *Archaeol. Prospect.* **2010**, *17*, 175–186. [[CrossRef](#)]
23. Sukhanov, D.Y.; Ponomarev, O.; Zavyalova, K.; Khmelev, V.; Roslyakov, S. Radar with a local positioning video-system. In Proceedings of the 2017 Progress in Electromagnetics Research Symposium-Spring (PIERS), St. Petersburg, Russia, 22–25 May 2017; pp. 3723–3728.
24. Kaniewski, P.; Kraszewski, T.; Pasek, P. UWB-Based Positioning System for Supporting Lightweight Handheld Ground-Penetrating Radar. In Proceedings of the 2019 IEEE International Conference on Microwaves, Antennas, Communications and Electronic Systems (COMCAS), Tel-Aviv, Israel, 4–6 November 2019; pp. 1–4.
25. Ciampoli, L.B.; Calvi, A.; Di Benedetto, A.; Fiani, M.; Gagliardi, V. Ground Penetrating Radar (GPR) and Mobile Laser Scanner (MLS) technologies for non-destructive analysis of transport infrastructures. In Proceedings of the Earth Resources and Environmental Remote Sensing/GIS Applications XII, Online, 13–18 September 2021; Volume 11863, pp. 166–174.
26. Merkle, D.; Frey, C.; Reiterer, A. Fusion of ground penetrating radar and laser scanning for infrastructure mapping. *J. Appl. Geod.* **2021**, *15*, 31–45. [[CrossRef](#)]
27. Grasmueck, M.; Viggiano, D.A. Integration of ground-penetrating radar and laser position sensors for real-time 3-D data fusion. *IEEE Trans. Geosci. Remote Sens.* **2006**, *45*, 130–137. [[CrossRef](#)]
28. Hui, C.K.; Luo, T.X.; Lai, W.W.; Chang, R.K. GPR mapping with mobile mapping sensing and tracking technologies. *Tunn. Undergr. Space Technol.* **2022**, *122*, 104362. [[CrossRef](#)]
29. Hjartarson, K. Dynamic Path Planning, Mapping, and Navigation for Autonomous GPR Survey Robots. Master’s Thesis, Umeå University, Umeå, Sweden, 2023.
30. Ogguniyi, S.; Withey, D.; Marais, S.; Crafford, G. LiDAR-based 3D mapping and localisation system for ground penetrating radar. In Proceedings of the 2020 International SAUPEC/RobMech/PRASA Conference, Cape Town, South Africa, 29–31 January 2020; pp. 1–6.

31. Wang, X.; Li, X.; Liao, J. Tightly-coupled stereo visual-inertial-LiDAR SLAM based on graph optimization. *Acta Geod. Cartogr. Sin.* **2022**, *51*, 1744.
32. Shan, T.; Englot, B.; Meyers, D.; Wang, W.; Rus, D. LIO-SAM: Tightly-coupled Lidar Inertial Odometry via Smoothing and Mapping. In Proceedings of the 2020 IEEE/RSJ International Conference on Intelligent Robots and Systems (IROS), Las Vegas, NV, USA, 24 October–24 January 2021.
33. Zhao, S.; Zhang, H.; Wang, P.; Nogueira, L.; Scherer, S. Super Odometry: IMU-centric LiDAR-Visual-Inertial Estimator for Challenging Environments. In Proceedings of the 2021 IEEE/RSJ International Conference on Intelligent Robots and Systems (IROS), Prague, Czech Republic, 27 September–1 October 2021.

Disclaimer/Publisher’s Note: The statements, opinions and data contained in all publications are solely those of the individual author(s) and contributor(s) and not of MDPI and/or the editor(s). MDPI and/or the editor(s) disclaim responsibility for any injury to people or property resulting from any ideas, methods, instructions or products referred to in the content.